ELSEVIER

Contents lists available at ScienceDirect

Materials Today Communications

journal homepage: www.elsevier.com/locate/mtcomm





Three-dimensional strength and stiffness optimization of coated structures with lattice infill

Zhichao Wang 1, Ali Y. Tamijani *,1

Embry-Riddle Aeronautical University, Daytona Beach, FL 32114, USA

ARTICLE INFO

Keywords: Topology optimization Homogenization Coated structures Additive manufacturing Stress optimization

ABSTRACT

Additive manufacturing (AM) offers a design freedom to fabricate high performance parts, such as a solid outer shell with a porous infill (coated structure), to enhance strength-to-weight ratio. The goal of this article is to describe and analyze how to develop a strength-based optimization to design the topology and infill microstructures density by minimizing the failure load subjected to weight constraint. To establish the coated structure, the material and coating indicators are obtained using double smoothing and projection of design variable. Additionally, three characteristic parameters are utilized to represent the lattice geometry. Two lattices, including octet-truss lattice and cubic lattice, are considered for the infill region. The strength-based optimization is developed based on Hill's yield criterion, and the element failure indices are aggregated to a single function using the p-mean approach. The proposed design methodology has been successfully applied to different numerical test cases, which showed that performing strength-based optimization led to a smoother boundary at the re-entrant corner and achieving a lower failure load. Numerical evaluation also demonstrated that, in contrast to solely considering characteristic parameters to design lattice, considering additional material and coating indicators during the design process resulted in optimized topology as well as infill microstructures material distribution.

1. Introduction

The focus of this study is on the design optimization of 3D coated structures with lattice infill to optimize strength/stiffness subjected to a volume constraint. In general, coated structures consist of a solid outer shell and a porous infill base structure. The infill pattern can be categorized into uniform and non-uniform. Clausen, Aage, and Sigmund [1] presented a density-based method to obtain a 2D stiffness optimized coated structure with isotropic infill. In their study, a single density per element was utilized to optimize both coating and base material. The density was filtered using the Helmholtz-type filtering approach [2] to obtain smooth density, and then it was projected using the smoothed Heaviside projection [3] to represent the base material. The projected density was filtered again, and the gradient of filtered based material represented the coating material. Later, the authors projected the 2D infill homogenized density to a triangular lattice, and they extruded the design in an out-of-plane direction [4]. The buckling load for Solid Isotropic Material Penalization (SIMP) and coated structures optimized designs were compared for the MBB beam. While the stiffness of optimized coated structure decreased by about 25 %, the buckling load was increased by more than five times. The observation of the out-of-plane buckling motivated the development of 3D shell structures with porous infill [5].

To generate a 3D non-uniform periodic lattice infill pattern, Lu et al. [6] employed a hollowing optimization algorithm by using the Voronoi partition of internal domain and creating honeycomb cells. The objective for optimization in their work was maximizing the strength-to-weight ratio, and the design variables included the size and material density of Voronoi cells. Hoang et al. [7] developed a framework based on adaptive geometric components to obtain 2D stiffness-based optimized coated structures with nonperiodic infill porosities. Two sets of bars were considered in the geometric components—one for the macrostructure coating and another for the micro-scale infill lattice. Three density functions were used to design the thickness of the coating and the density of the infill lattice. It was shown that the coated structures with nonuniform coating thickness and nonuniform infill had lower compliance than the coated structures with uniform coating and infill. Further, Wu et al. [8] presented a modified

E-mail addresses: wangz6@my.erau.edu (Z. Wang), ali.tamijani@erau.edu (A.Y. Tamijani).

^{*} Corresponding author.

Aerospace Engineering Department.

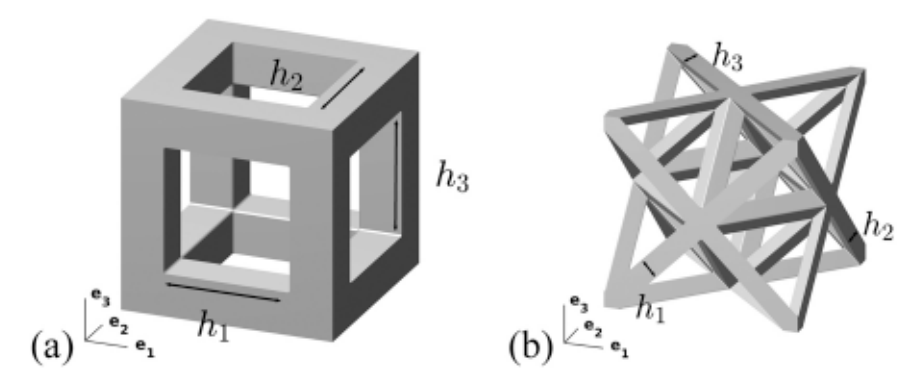


Fig. 1. Characterizing parameters for (a) cubic lattice and (b) octet-truss lattice.

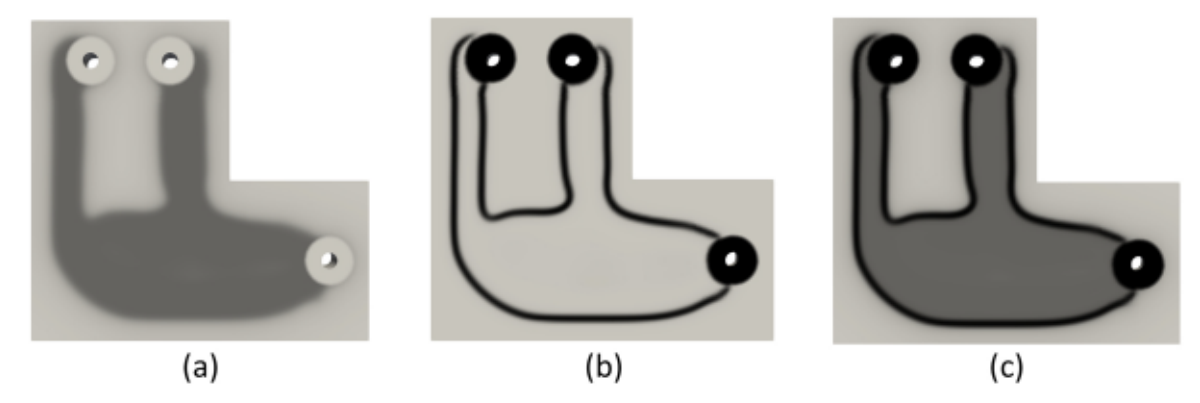


Fig. 2. (a) Material indicator variable (φ) ; (b) coating thickness (τ) ; and (c) density distribution $(\rho(\varphi, \tau))$.

SIMP approach with a p-mean aggregation of local volume fraction constraints to obtain a 3D stiffness optimized non-uniform infill pattern. The optimized porous infill resembled trabecular bone architecture. They compared their results with the honeycomb structure obtained using the hollowing optimization algorithm [6], and showed that the stiffness of porous infill was 50% higher than the honeycomb structure.

Level set optimization has also been used to obtain coated structures. Dapogny et al. [9] performed 2D stiffness-based shape optimization of coated structures with infill material. Four infill types were considered in this study: isotropic infill material, anisotropic infill pattern, infill with offset pattern, and customized or optimized infill pattern. The performance of various infill types was compared with SIMP. It was shown that for the cases with varying principal stress directions in different regions, the designs with an anisotropic infill pattern lowered optimized weight when compared with isotropic infill.

Motivated by the work of Pantz and Trabelsi [10], Groen, Wu, and Sigmund [11] developed a homogenization-based stiffness optimization for 2D coated structures with lattice infill. Four sets of design variables were used to represent the coating and base materials, the geometry of microstructures, and the orientation of unit-cell. The homogenized infill was projected using a square cell with a rectangular hole. The projection using the mapping functions based on optimized orientation resulted in variation of lattice spacing in the design domain. Thus, the authors implemented an adaptive periodicity scheme to obtain a more regular infill pattern. Geoffroy-Donders et al. [12] utilized 2D homogenization-based level set optimization to obtain the outer shape and periodic infill lattice pattern. In contrast to the classical level set optimization, where shape derivative is only present on the boundary, due to the changes in the shape and internal material of the coated structures, the shape derivatives were present both on the boundary and inside the shape. This could result in a discontinuous velocity field obtained from shape derivatives. Thus, the velocity field was obtained from the regularization of shape derivatives.

While the stiffness-based optimization of coated structures with periodic lattice infill has received considerable attention, their strength-based optimization has not been previously studied. In the related context of lattice structures without coating, the stress-constrained optimization has been performed based on two methods—the effective allowable stresses and amplifying the homogenized stress. Donders [13] utilized an amplification factor to scale the homogenized stress of lattice structures. Cheng, Bai, and To [14] implemented effective yield strength in Hill's model to perform topology optimization of lattice structures with stress constraints. Yu et al. [15] investigated the stress constrained topology optimization of shell-lattice structures using von Mises and Tsai-Hill yield criteria for the shell and infill lattice, respectively.

The goal of our current work is to obtain the coating thickness and lattice infill distribution for optimized strength/stiffness. We previously investigated the compliance-based lattice structure topology and morphology optimization [16–18]. We also included the stress constraint using the modified Hill's yield criterion in the optimization framework [19]. An observation from our previous study of lattice structures was that while we didn't consider the outer surface coating, the outer surface converged to a solid, especially for the case of stress-based optimization, to reduce the failure load. This observation motivated us to study the strength-based optimization of coated structures with lattice infill.

In our current study, the infill region of coated structures consists of microscopic periodic lattice. The effective properties are obtained using numerical homogenization. Two lattices, including octet-truss lattice and cubic lattice, are considered for the infill region. To establish the coated structure, the material and coating indicators were obtained using double smoothing and projection of design variables. Additionally, three characteristic parameters were utilized to represent the lattice geometry. Two sets of problems were investigated for numerical examples: (a) keeping the characteristic parameters constant and optimizing the design variable to obtain the optimized topology of coated

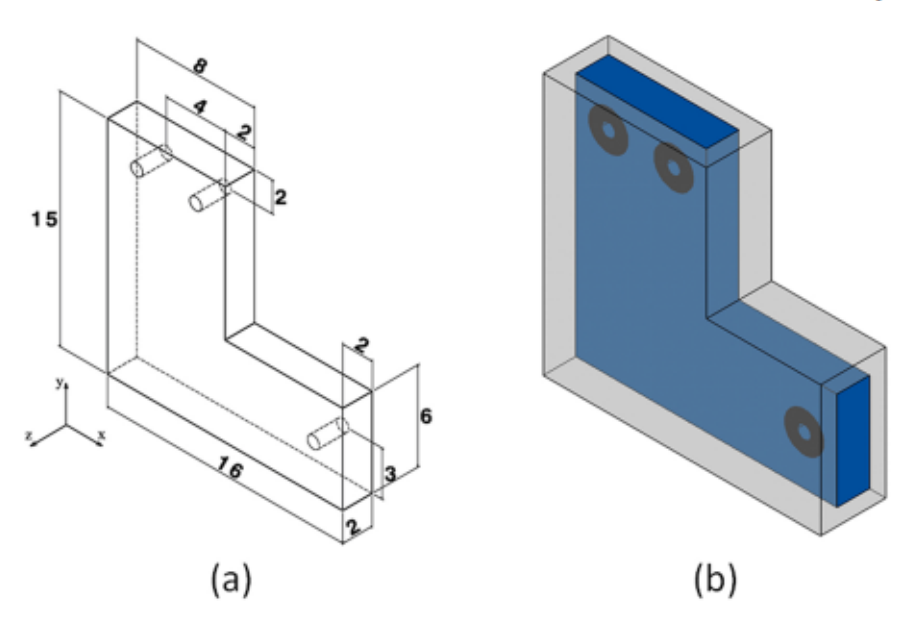


Fig. 3. (a) Dimension of the L-bracket with holes; (b) the design domain (blue) with the extended region (gray).

Table 1

P-mean failure index γ_p , compliance, maximum Hill's stress and volume fraction for the cubic lattice compliance-based and strength-based optimizations.

Optimised design	P-mean failure index γ_p	Compliance	Maximum Hill's stress	Volume fraction
Strength-based optimization with varied h_l	0.056	0.032	0.099	0.3
Strength-based optimization with fixed h	0.105	0.039	0.200	0.3
Compliance-based optimization with varied h_i	0.219	0.028	0.500	0.3
Compliance-based optimization with fixed h_i	0.329	0.034	0.760	0.3

structures with uniform material distribution in the infill region, and (b) considering the characteristic parameters as design variables to obtain non-uniform lattice. The optimized designs for these two cases were compared. The strength-based optimization was developed based on the Hill's yield criterion, and the element failure indices were aggregated to a single function using the p-mean approach. The results of strength-based optimizations were compared with those obtained for compliance-based optimization, and the reduction in failure load using the former was validated. The result of strength-based optimization of coated structures was also compared with lattice structures without coating and the advantages of using solid outer shell are discussed.

2. Theoretical background

The infill region of coated structures consists of microscopic periodic cells. The topology optimization framework is based on the homogenized properties of microlattices. The process of parameterization of various cell types and lattices and the calculation of homogenized properties have been discussed in our prior research studies [17–19]. The characterizing parameters (h_1, h_2, h_3) were selected to establish the lattice geometry (Fig. 1). The homogenized stiffness tensor $(\overline{\mathbf{C}}(h_1, h_2, h_3))$ and macroscopic effective yield stresses $(\overline{\mathbf{O}}^{Y}(h_1, h_2, h_3))$ were obtained using numerical homogenization. The infill density function $\rho^I(h_1, h_2, h_3)$ can be calculated analytically for cubic lattice $(\overline{\rho}(h_1, h_2, h_3) = (1 - h_1h_2 - h_1h_3 - h_2h_3 + 2h_1h_2h_3))$ or numerically for octet-truss lattice

[18]. These properties are implemented in the optimization framework. The stiffness tensor (C^0) and yield stresses (σ^Y) for solid coating are obtained based on the material properties.

In order to establish the coated structures, we followed the procedure presented in [1,11]. A material indicator variable (φ) was introduced to represent the base structure (see Fig. 2(a)). The material indicator variable was obtained from double smoothing and projection (DSP) of design variable μ . The filter radius (R_1) and projection parameters β_1 and η_1 are similar for both steps in DSP. Then, the coating thickness (τ) is obtained from the smoothing and projection of φ with filter radius (R_2) .

 $R_2 < R_1$) and projection parameters β_2 and η_2 (see Fig. 2(b)). It was shown in [1] that R_2 can be related to the reference coating thickness (t_{ref}) by $R_2 \approx 2.5 t_{ref}$.

The Helmholtz-type filtering [2] and smoothed Heaviside projection [3] are utilized for the smoothing and projection operations. The homogeneous Neumann boundary conditions in Helmholtz-type filtering equation cause issues close to the boundary. A padding approach is proposed to resolve the boundary effect [11,20,21]. In this approach, the boundary of the design domain is extended $(d_{\rm ext})$ except at the support and load regions. The stiffness tensor in the extended region is multiplied by a parameter q to ensure the optimized design remains in the original design domain [11]. In the current study, q=0.1 has shown to work the best for the test cases.

The stiffness tensor and density are defined based on the coating and infill [11]:

$$\mathbf{C}(\varphi, \tau, \mathbf{h}_1, \mathbf{h}_2, \mathbf{h}_3) = 10^{-9} \mathbf{C}^0 + q(\overline{\mathbf{C}}(\mathbf{h}_1, \mathbf{h}_2, \mathbf{h}_3) - 10^{-9} \mathbf{C}^0) \varphi^{p_1} + q(\mathbf{C}^0 - \overline{\mathbf{C}}(\mathbf{h}_1, \mathbf{h}_2, \mathbf{h}_3) \varphi^{p_1}) \tau^{p_2}$$
(1)

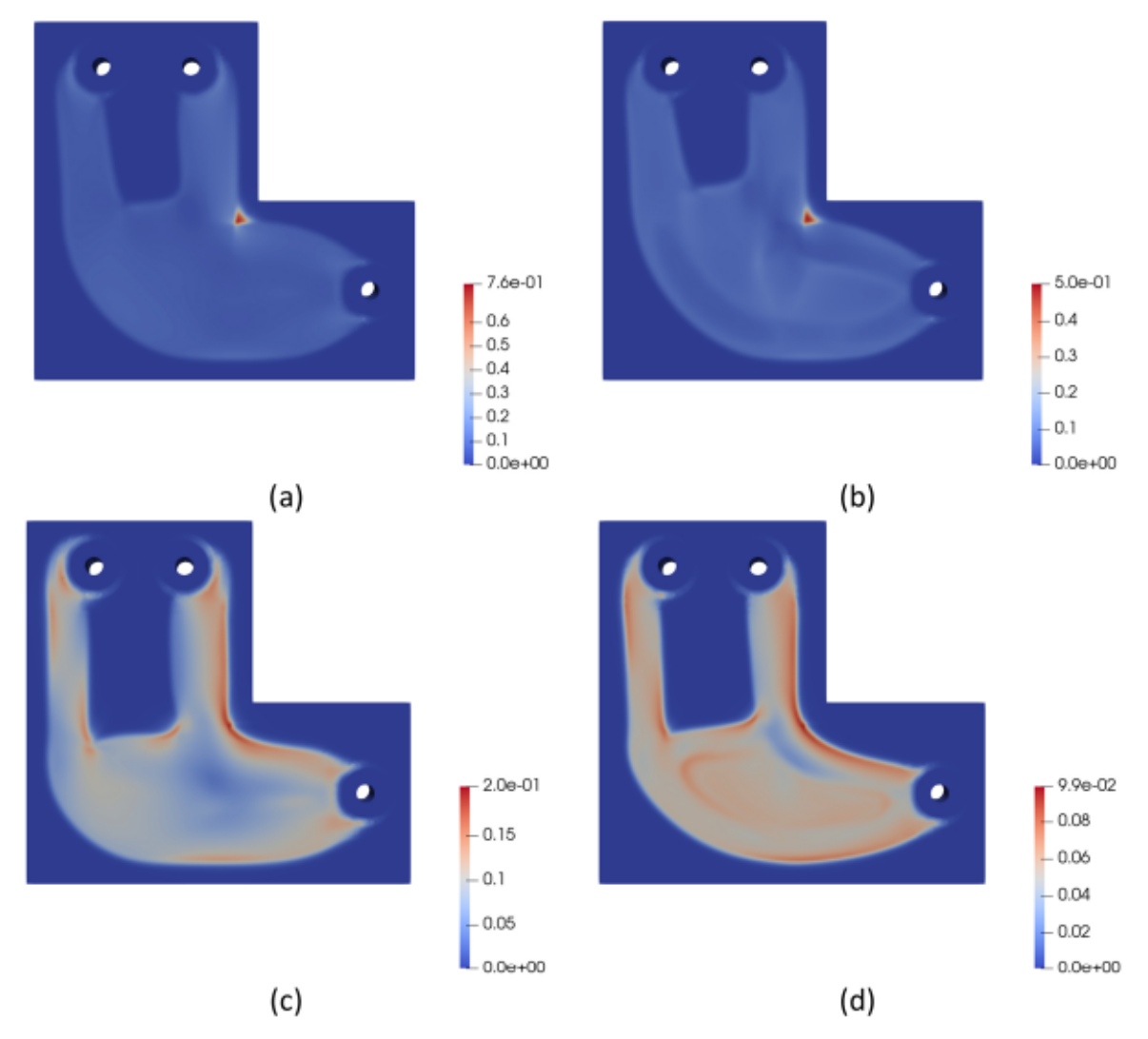


Fig. 4. Hill's stress distribution of the y-cross-section for the cubic lattice (a) fixed microstructure density compliance-based optimization; (b) varied microstructure density strength-based optimization; (c) fixed microstructure density strength-based optimization;

$$\rho(\varphi, \tau, h_1, h_2, h_3) = \overline{\rho}(h_1, h_2, h_3)\varphi + (1 - \overline{\rho}(h_1, h_2, h_3)\varphi)$$
 (2)

where p_1 and p_2 are the penalty parameters related to the material indicator and coating thickness. The element failure index vector (γ_e) is defined based on the Hill's yield criterion.

$$\gamma_e = \sqrt{\sigma^T V \sigma}$$

$$V_{11} = \left(\frac{1}{\overline{\sigma}_{11}^{\gamma}}\right)^2, V_{22} = \left(\frac{1}{\overline{\sigma}_{22}^{\gamma}}\right)^2, V_{33} = \left(\frac{1}{\overline{\sigma}_{32}^{\gamma}}\right)^2$$

$$\mathbb{V}_{12} = -\frac{1}{2} \Biggl(\left(\frac{1}{\overline{\sigma}_{11}^Y} \right)^2 + \left(\frac{1}{\overline{\sigma}_{22}^Y} \right)^2 - \left(\frac{1}{\overline{\sigma}_{33}^Y} \right)^2 \Biggr),$$

$$V_{13} = -\frac{1}{2} \left(\left(\frac{1}{\overline{\sigma}_{11}^{Y}} \right)^{2} + \left(\frac{1}{\overline{\sigma}_{33}^{Y}} \right)^{2} - \left(\frac{1}{\overline{\sigma}_{22}^{Y}} \right)^{2} \right), \tag{3}$$

$$\mathbb{V}_{23} = -\frac{1}{2} \left(\left(\frac{1}{\overline{\sigma}_{22}^Y} \right)^2 + \left(\frac{1}{\overline{\sigma}_{33}^Y} \right)^2 - \left(\frac{1}{\overline{\sigma}_{11}^Y} \right)^2 \right)$$

For the coating region, the stress is $\sigma = \mathbb{C}^0 \varepsilon$ and the yield stress is $\overline{\sigma}^Y = \sigma^Y$. For the infill region, $\sigma = \overline{\mathbb{C}} \varepsilon$ (ε is the macroscopic strain), and

the effective yield stress, $\overline{\sigma}^Y$, is a function of characteristic parameters (h_1, h_2, h_3) [18]. The ϵ -relaxed approach [22] is adopted to address the stress singularities at low densities. The following stress interpolation function is introduced for the coating and infill material distribution:

$$\eta_F = \frac{\varphi}{\epsilon(1-\varphi) + \varphi} + \left(1 - \frac{\varphi}{\epsilon(1-\varphi) + \varphi}\right) \frac{\tau}{\epsilon(1-\tau) + \tau}$$
(4)

where $\epsilon = 0.2$ is selected in this work. The relaxed failure index is then introduced by utilizing the stress interpolation function:

$$\gamma_e^{\ r} = \eta_F \gamma_e$$
 (5)

The element failure indices are aggregated to a single function using the powers function [23]:

$$\gamma_p = \left(\left(\frac{1}{\Omega} \right) \int_{\Omega_n} (\gamma_e^r)^p d\Omega \right)^{\frac{1}{p}}$$
(6)

where Ω is the volume of design domain, p is a tuning coefficient, and p = 10 is selected for the test cases in this study.

Two optimization problems are considered in this research: (1) minimizing the compliance $(J = \int_{\Omega} e^{T}(u)Ce(u)dx)$ subjected to the equilibrium equation and volume fraction constraint (g), and (2) minimizing the p-mean failure function $(J = \gamma_p)$ subjected to the equilibrium

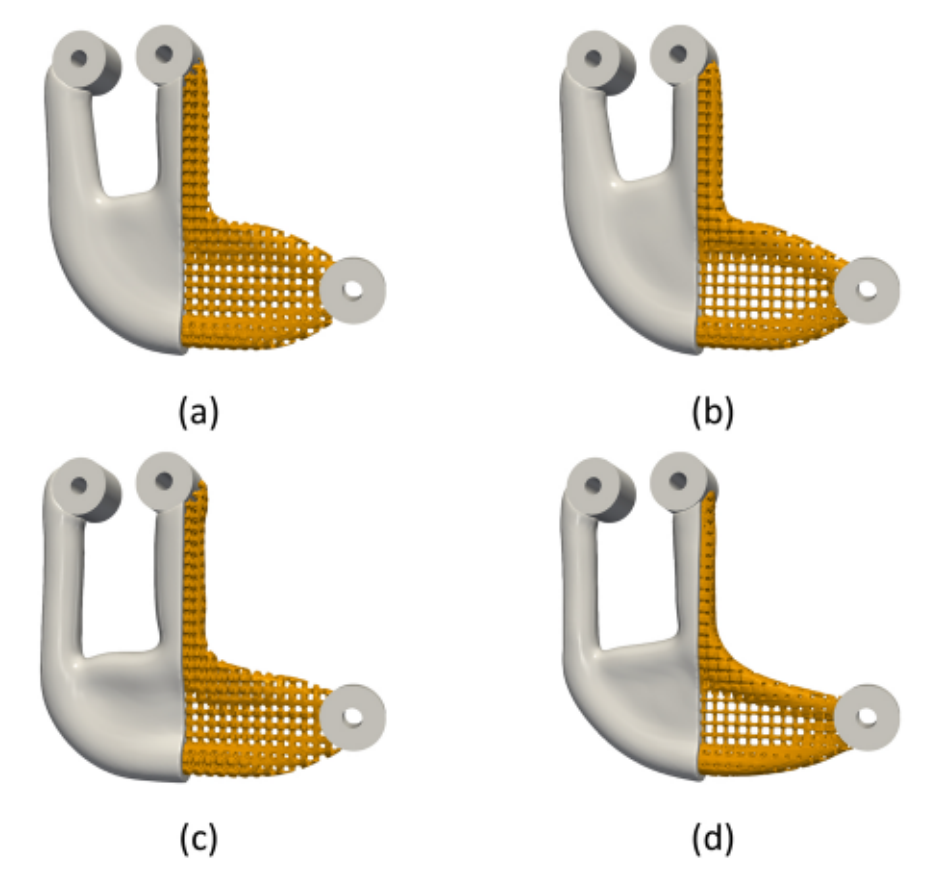


Fig. 5. The coated structures with projected cubic lattice of compliance-based optimization with (a) fixed and (b) varied h_1 , strength -based optimization with fixed (a) fixed and (b) varied h_1 .

Table 2

P-mean failure index γ_p , compliance, maximum Hill's stress and volume fraction for the octet-truss lattice compliance-based and strength-based optimizations.

Optimized design	P-mean failure index γ _p	Compliance	Maximum Hill's stress	Volume fraction
Strength-based optimization with varied h _l	0.048	0.031	0.089	0.3
Strength-based optimization with fixed h _i	0.107	0.053	0.210	0.3
Compliance-based optimisation with varied h _l	0.208	0.027	0.490	0.3
Compliance-based optimization with fixed h _l	0.355	0.043	0.830	0.3

equation and volume fraction constraint. The optimization statement is listed below:

 $\min J(\mu, h_1, h_2, h_3, \mathbf{u})$

$$\text{subjected to} \left\{ \begin{array}{l} \int_{\Omega} \ \boldsymbol{\varepsilon}^T(\boldsymbol{u}) C \boldsymbol{\varepsilon}(\boldsymbol{v}) d\boldsymbol{x} = \int_{\Gamma_N} \ \boldsymbol{f}^T \boldsymbol{v} d\boldsymbol{x} \\ \\ g = \left(\frac{1}{\Omega}\right) \int_{\Omega} \ \rho(\boldsymbol{\mu}, \boldsymbol{h}_1, \boldsymbol{h}_2, \boldsymbol{h}_3) d\Omega - V_g \leq 0 \end{array} \right\}$$

design variables
$$0 < h_n$$
 and $\mu \le 1$, $n = 1, 2, 3$ (7)

where V_g is the upper bound of the volume constraint, f is tractions on boundary Γ_N , and ν is the virtual displacement field. An alternative strength-based optimization problem could be formulated based on minimizing the volume fraction subjected to failure constraint:

$$\min\left(\frac{1}{\Omega}\right)\int_{\Omega} \rho(\mu, \mathbf{h}_1, \mathbf{h}_2, \mathbf{h}_3)d\Omega$$

subjected
$$to \left\{ \int_{\Omega} e^{T}(u)Ce(v)dx = \int_{\Gamma_{N}} f^{T}vdx \right\}$$

design variables
$$0 < h_n$$
 and $\mu \le 1$. $n = 1, 2, 3$ (8)

Since the goal of the current study is to compare the stiffness and maximum Hill's stress for compliance and strength-based optimizations using the same volume constraint, we focused on the optimization statement (7). The sensitivity analyses for volume fraction constraint, the compliance objective function, and the p-mean failure objective function are required in the optimization process. The sensitivity of the volume fraction is:

$$\frac{dg}{d\mu_{\epsilon}} = \left(\frac{1}{\Omega}\right) \frac{d\rho_{\epsilon}}{d\mu_{\epsilon}} \Omega_{\epsilon}$$

$$\frac{dg}{dh_{--}} = \left(\frac{1}{\Omega}\right) \frac{d\rho_{e}}{dh_{--}} \Omega_{e} \tag{9}$$

The adjoint method is utilized to obtain the sensitivity of objective functions. The compliance objective function is self-adjoint, thus

$$\frac{d\mathbf{J}}{\partial \mu_{\epsilon}} = -\int_{\Omega_{\epsilon}} \mathbf{e}^{T}(\mathbf{u}) \frac{d\mathbf{C}_{\epsilon}}{d\mu_{\epsilon}} \mathbf{e}(\mathbf{u}) d\Omega_{\epsilon}$$

$$\frac{\partial J}{\partial h_{ne}} = -\int_{\Omega_{e}} e^{T}(u) \frac{dC_{e}}{dh_{ne}} e(u) d\Omega_{e}$$
(10)

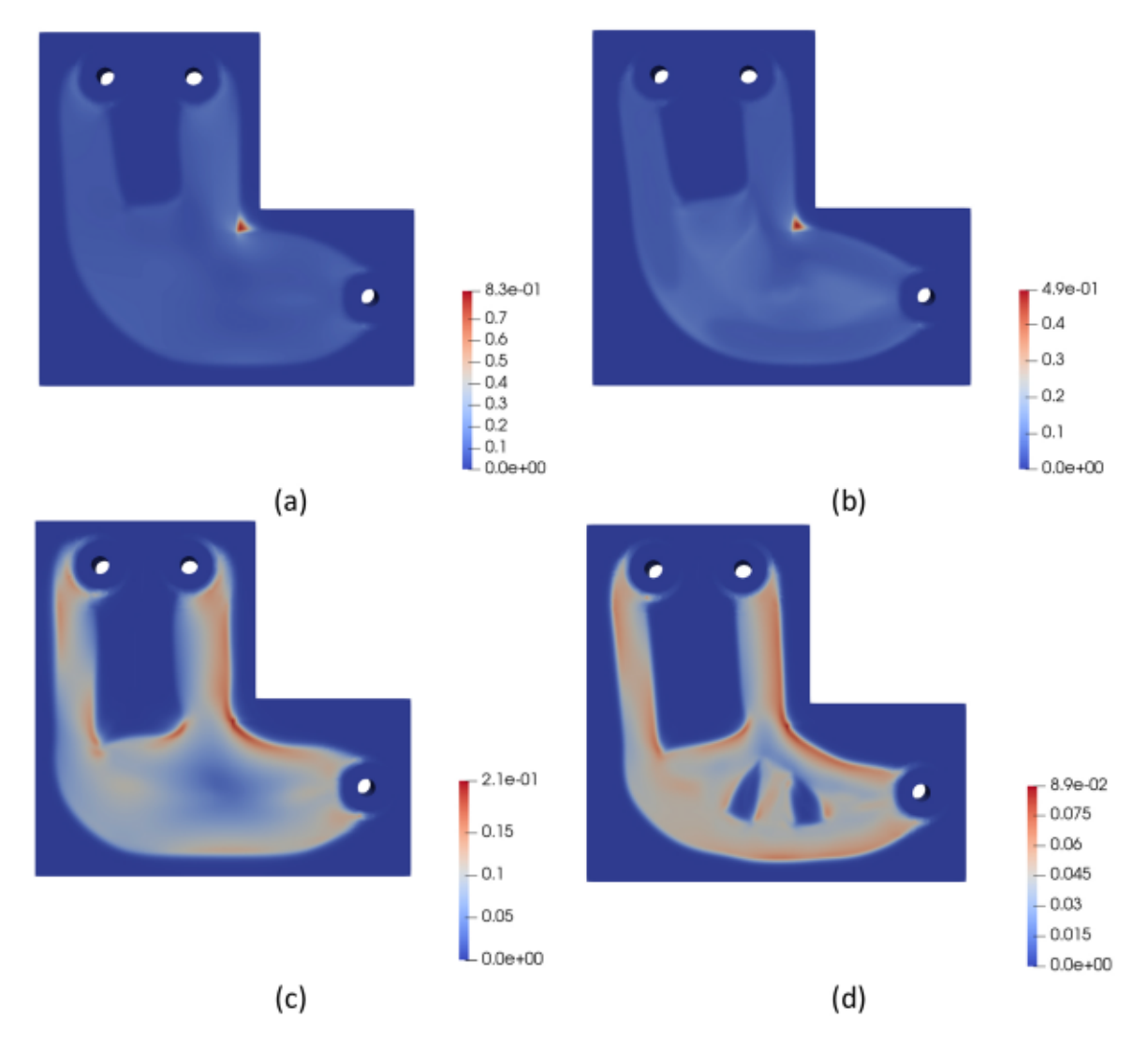


Fig. 6. Hill's stress distribution of the y-cross-section for the octet-truss lattice (a) fixed microstructure density compliance-based optimization; (b) varied microstructure density compliance-based optimization; (c) fixed microstructure density strength-based optimization; (d) varied microstructure density strength-based optimization.

For the stress objective function, the Lagrangian is constructed to find the adjoint equation and perform sensitivity. The Lagrangian for the p-mean failure objective function is:

$$L = \gamma_p + \int_{\Omega} e^T(u) C e(v) dx - \int_{\Gamma_v} f^T v d\Gamma \qquad (11)$$

Then, the derivative of the Lagrangian with respect to μ_e is:

$$\frac{dL}{d\mu_{\epsilon}} = \left(\frac{1}{\Omega}\right) \int_{\Omega_{\epsilon}} \gamma_{p}^{1-p} (\gamma_{\epsilon}')^{p-1} \left(\frac{d\eta_{F}}{d\mu_{\epsilon}} \gamma_{\epsilon} + \eta_{F} \frac{1}{\gamma_{\epsilon}} \sigma^{T} \nabla \overline{C} \varepsilon(u')\right) d\Omega_{\epsilon}
+ \int_{\Omega_{\epsilon}} \varepsilon^{T}(u) \frac{dC_{\epsilon}}{d\mu_{\epsilon}} \varepsilon(v) d\Omega_{\epsilon} + \int_{\Omega} \varepsilon^{T}(u') C \varepsilon(v) d\Omega + \int_{\Omega} \varepsilon^{T}(u) C \varepsilon(v') d\Omega
- \int_{\Gamma_{N}} f^{T} v' d\Gamma$$
(12)

Imposing the equilibrium equation, and collecting the terms including u' results in adjoint equation:

$$\left(\frac{1}{\Omega}\right)\int_{\Omega} \gamma_p^{1-p}(\gamma_e)^{p-1} \eta_F \frac{1}{\gamma_e} \sigma^T \nabla \overline{C} \varepsilon(u') d\Omega + \int_{\Omega} \varepsilon^T(u') C \varepsilon(v) d\Omega = 0$$
 (13)

After finding the adjoint variable ν from the equation above, the sensitivity of the p-mean failure objective function is obtained:

$$\frac{dJ}{d\mu_{\epsilon}} = \frac{dL}{d\mu_{\epsilon}} = \left(\frac{1}{\Omega}\right) \int_{\Omega_{\epsilon}} \gamma_{p}^{1-p} (\gamma_{\epsilon}^{r})^{p-1} \frac{d\eta_{F}}{d\mu_{\epsilon}} \gamma_{\epsilon} \quad d\Omega_{\epsilon} + \int_{\Omega_{\epsilon}} \varepsilon^{T}(u) \frac{dC_{\epsilon}}{d\mu_{\epsilon}} \varepsilon(v) d\Omega_{\epsilon}$$
(14)

The sensitivity of the p-mean failure objective function with respect to h_{ne} is obtained by following the same procedure:

$$\frac{dJ}{dh_{ne}} = \left(\frac{1}{\Omega}\right) \int_{\Omega_{\epsilon}} \gamma_{p}^{1-p} (\gamma_{\epsilon}')^{p-1} n_{F} \frac{1}{\gamma_{\epsilon}} \left(\sigma^{T} \nabla \frac{d\overline{C}}{dh_{ne}} \varepsilon(v) + \sigma^{T} \frac{d\nabla}{dh_{ne}} \sigma\right) d\Omega_{\epsilon} \\
+ \int_{\Omega} \varepsilon^{T} (u) \frac{dC_{\epsilon}}{dh_{ne}} \varepsilon(v) d\Omega_{\epsilon}$$
(15)

The optimization problems are solved using the method of moving asymptotes [24]. The analysis and optimization frameworks are developed using the open-source PDE solver FreeFem+ + [25]. The displacements and adjoint variables are discretized using P_1 -functions. All other variables, such as characteristic parameters, material indicator, and coating thickness are discretized using P_0 -functions.

3. Numerical examples

A 3D L-bracket with holes to apply loading and boundary conditions is used as a benchmarked problem. The dimension is shown in Fig. 3(a).

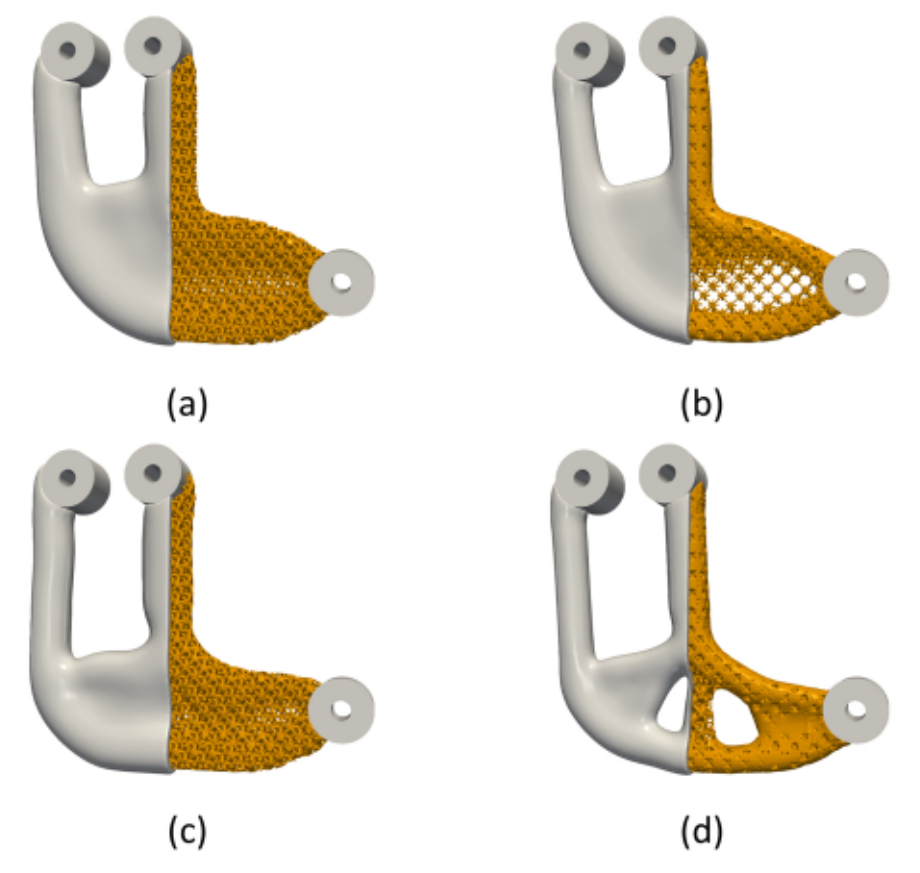


Fig. 7. The coated structures with projected octet-truss lattice of compliance-based optimization with (a) fixed and (b) varied h_i , strength -based optimization with fixed (a) fixed and (b) varied h_i .

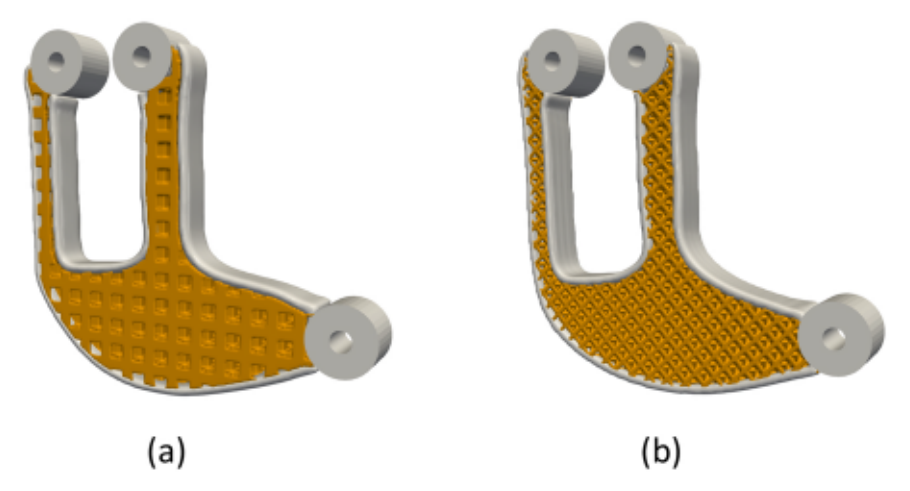


Fig. 8. The projected designs without side coating for (a) cubic lattice with the periodicity of 1 and (b) the octet-truss lattice with the periodicity of 0.8.

The bracket contains three holes, and they have a radius of 0.4. A downward 0.15 pressure was applied on the surface of the bottom hole, while two holes at the top were clamped. The volume fraction is set as 30 %. This domain was covered by an extended region (see Fig. 3(b)). The design domain and the extended region were discretized by 3.6 million tetrahedral elements. The material around the holes with 0.8 radius extension was fixed as solid during the optimization (see the black region in Fig. 3(b)).

The Young's modulus of the material used for the L-bracket is 1288.3 and the Poisson ratio is 0.375. The yield strength σ^Y is 18.3, and the P-mean parameter is p=10.

Two sets of strength-based optimizations with fixed and varied

microstructure density were performed for cubic and octet-truss lattices. The compliance designs were also obtained to demonstrate the improvement of Hill's stress distribution by performing the strength-based optimization. The maximum number of iterations is 1000. The optimized designs were obtained by using the HB120rs v2 virtual machine of Microsoft Azure. It features 120 AMD EPYC 7002-series CPU cores, 480 GB of RAM and 480 MB of L3 cache. The strength-based optimization with varied and fixed microstructure densities were achieved by using the virtual machine in 48 h and 32 h, respectively.

For the cubic lattice, the first filtering radius R_1 is 1.25, the second filtering radius R_2 is 0.5 and the reference coating thickness (t_{ref}) is 0.2. The thickness of the extended region is $d_{ext} = R_1$. The low and up limits

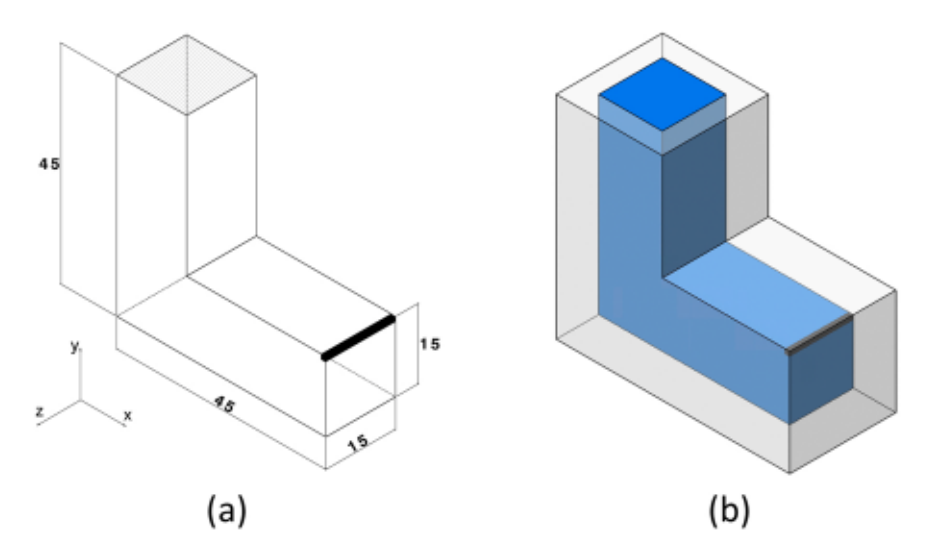


Fig. 9. (a) Dimension of the L-bracket (mm) [14]; (b) the design domain (blue) with the extended region (gray).

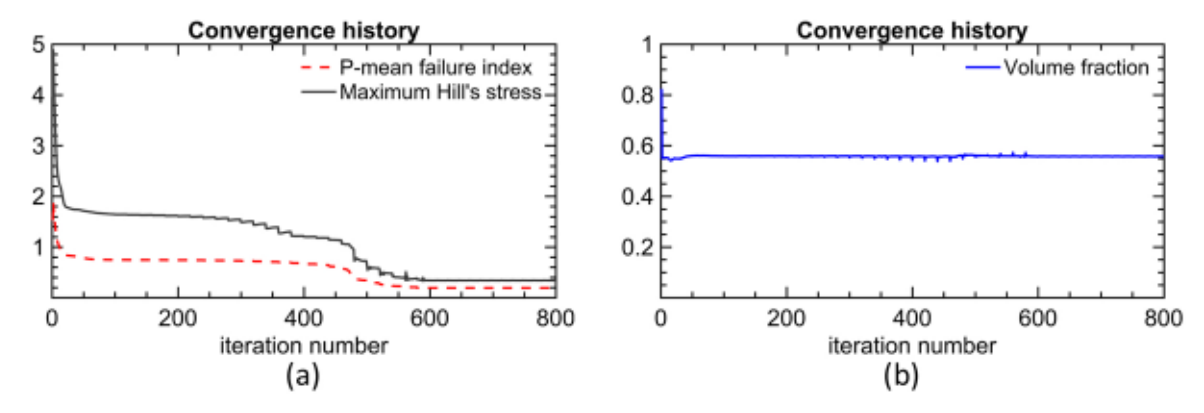


Fig. 10. Convergence history of (a) P-mean failure index γ_p , maximum Hill's stress; and (b) volume fraction of the L-bracket test case.

for the varied microstructure density are set at [0.2]6, 0.896]. Thus, the range of characteristic parameters (h_i) is [0.2, 0.7]. For the case with fixed microstructure density, $h_i = 0.5$.

Table 1 shows the optimized P-mean failure index γ_p , compliance, maximum Hill's stress, and volume fraction for the cubic lattice for the strength and compliance-based optimizations. The Hill's stress distribution of the y cross-section for each optimization problem is shown in Fig. 4. For both strength-based and compliance-based designs, the varied density results in lower compliance and Hill's stress. As can be seen in Fig. 4, the stress concentration in the optimized compliance designs is removed in the strength-based designs, and thus a lower maximum Hill's stress is obtained. Fig. 5 shows the projected cubic lattices for the compliance-based and strength-based designs with a periodicity parameter of 0.5. The details of the projection steps are discussed in our prior publication [18]. A post-processing procedure is required to ensure the manufacturability of the projected lattice. The post-processing procedure is performed in multiple steps based on the minimum manufacturable feature size. First, a lattice is created based on manufacturable thickness, and then regions are created from the complement of the union between this lattice and the projected shape. Then, the regions with inscribed circle diameters (a measurement of porosity) less than manufacturable thickness are filled. The details of the post-processing procedure are reported in our prior publication [17].

For the octet-truss lattice, the range of h_i for the varied microstructure density problem is set as [0.15,0.65]. For the fixed microstructure density problem, h_i is set at 0.33 to achieve the same density as the cubic lattice. From the previous study of Young's modulus effective surfaces for various orientations [18], we know that the octet-truss lattice

properties are closer to a sphere for intermediate densities than those of the cubic lattice. Therefore, the first filtering R_1 for the octet-truss fixed microstructure density is slightly increased (R_1 =1.5) to prevent the design from converging into a SIMP solid-void design. Table 2 shows the optimized P-mean failure index γ_p , compliance, maximum Hill's stress and volume fraction of the octet-truss lattice for both strength and compliance-based designs. This table demonstrates the same trend that was seen in cubic lattice cases.

The Hill's stress distributions of the v cross-section for each octettruss case are shown in Fig. 6, and the corresponding projected lattices with the periodicity of 0.8 are shown in Fig. 7. Since the octet-truss lattice provides weaker orthotropic properties compared to cubic lattice, the strength-based optimized infill density distribution (Fig. 7(d)) is more like a SIMP design. Due to the orthotropic properties of cubic lattice at intermediate density, it is sensitive to the orientation. Since the orientation is fixed in this study, the failure index γ_p , maximum Hill's stress, and compliance are lower for the octet-truss lattice. The fixed microstructure density case of the octet-truss yields slightly higher optimized results than the cubic lattice due to utilizing a larger filtering parameter. One issue with the 3D solid coating is the powder trapping for the laser powder bed fusion additive manufacturing (L-PBF-AM). One approach to address this issue is to remove the extended region on the two sides in the x-y plan (see Fig. 3). The octet-truss and cubic lattice designs without the side coating are demonstrated in Fig. 8. It should be noted that the optimized design presented in Fig. 8 has lower out-ofplane bending stiffness compared to the optimized designs in Fig. 5 and Fig. 7. If out-of-plan stiffness is critical to the system requirement,

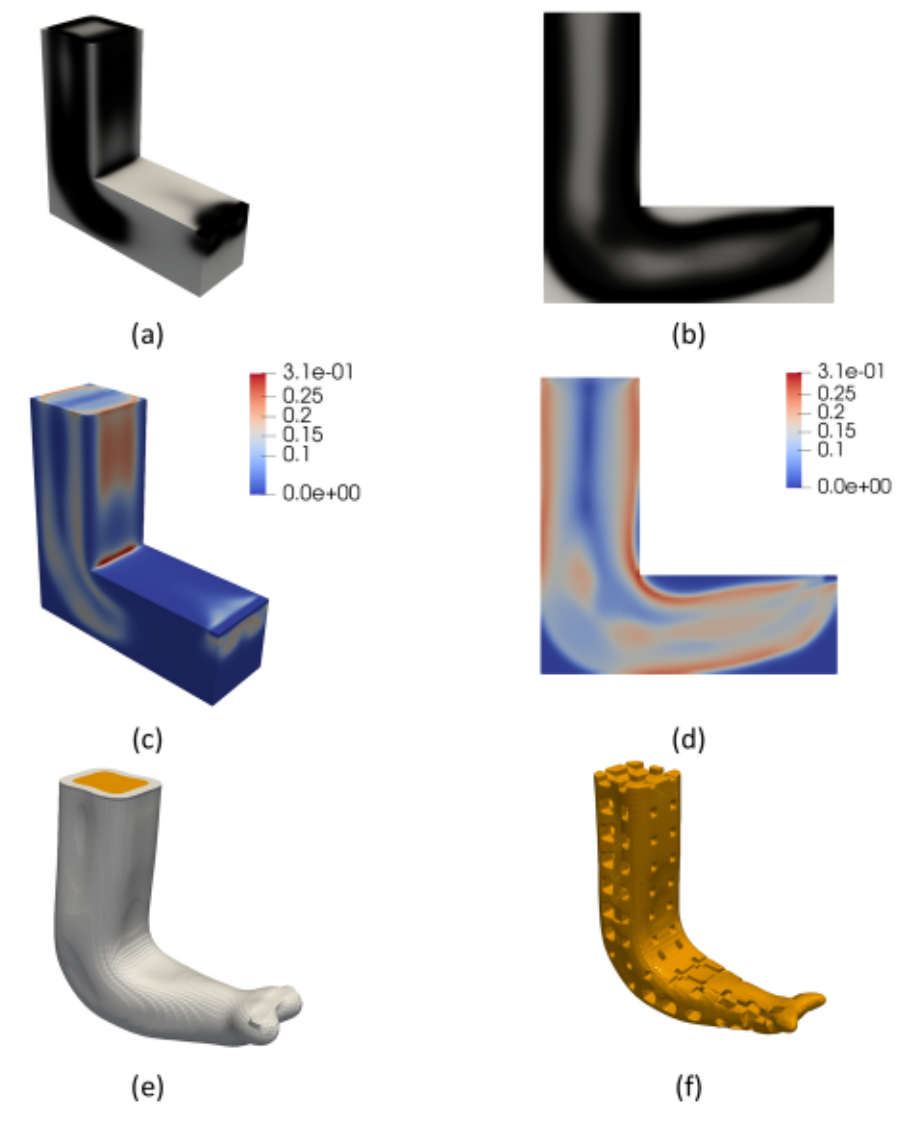


Fig. 11. (a) The density distribution; (b) the density distribution of the y-cross-section; (c) the Hill's stress distribution; (d) the Hill's stress distribution of the y-cross-section on the original mesh; (e) the coated structure with lattice infill; (f) the projected lattice infill.

then holes can be inserted in the coating to remove the powder.

Another L-bracket was optimized with the cubic lattice to compare the results with those reported by Cheng, Bai, and To [14]. Cheng, Bai, and To minimized the volume fraction subject to failure index constraint for lattice structures. In our current study, the objective function is the P-mean failure index γ_p , subject to volume constraint for coated structures with lattice infill. Thus, in this study, we investigated how these differences influence the optimized design and its corresponding failure index. The Young's modulus is given as 1745 MPa, Poisson ratio is 0.3 and the yield strength σ^{Y} is 65 MPa. The dimension of the baseline design is given in Fig. 9(a). It has a $15 \times 15 \text{ mm}^2$ cross-section, and its side length is given as 45 mm. A 130 N downward load was distributed at the top surface of the black region with an area of 2×15 mm². The top surface is clamped. During the optimization, the black region of Fig. 9(a) is fixed as solid with a volume of $2 \times 15 \times 1$ mm³. Cheng, Bai, and To [14] utilized a mesh with 16,875 eight-node hexahedron elements and reported an optimized volume fraction of 0.56 and maximum Hill' stress of 0.989.

An extended region covering the surrounding of the design domain is considered in our study (see Fig. 9(b)). The thickness of the extended region is $d_{\rm ext}=R_1$. The first and second filtering parameters are $R_1=6.37$ mm and $R_2=4.25$ mm, and the coating thickness is 1.7 mm. The

range of h_i is set as [0.1,0.6] due to the high volume fraction of 0.56. The strength-based design is obtained in 800 iterations. The design domain and extended region are discretized by 3.50 million tetrahedral elements. The convergence history of the P-mean failure index, maximum Hill's stress, and volume fraction are illustrated in Fig. 10. As can be seen, the P-mean failure index γ_p is reduced from 1.52 for the baseline design to 0.19 for optimized design, while the maximum Hill's stress is reduced from 3.86 to 0.31. The initial volume fraction is given as 0.82 and the volume fraction constraint of 0.56 is satisfied for the converged design

In Cheng, Bai, and To's study [14], the high density in the left region is only observed in the z-y vertical surfaces. In our current study, due to using coating solid in the outer shell, the higher infill density is obtained in both z-y and x-y planes (see Fig. 11 (a)). The Hill's stress shows a similar distribution trend as found by Cheng, Bai, and To [14] (see Fig. 11 (c)). However, due to the advantage of using extended region and coated structure in the current study, the boundary curve is smoother at the re-entrant corner, see Fig. 11 (e), to avoid stress concentration (see Fig. 11 (d)). The shape is not optimized in [14] due to not allowing the characterization parameters to approach zero. In the current study, the material indicator is utilized, which allows the optimization of shape. The maximum Hill's stress is 0.31 which is significantly lower than the

0.989 reported in [14]. This substantial improvement can be due to (a) the advantage of using extended region and coated structure; (b) a finer mesh utilized in the current study; (c) the difference of the objective and constraints considered during the optimization; and (d) the optimized shape from using the material indicator. Fig. 11 (f) shows the final projected results of the strength-based optimization by using the periodicity of 5 mm.

4. Conclusion

A homogenization-based topology optimization to design coated structures with lattice infill is presented in this article. The strengthbased and compliance-based optimization for two lattices, i.e. cubic lattice and octet-truss lattice, with fixed and varied microstructure densities are presented. The strength-based optimization is developed based on the Hill's yield criterion and the element failure indices are aggregated to a single function using the P-mean approach. Two case studies based on the L-shape bracket are presented. It was shown that preformatting strength-based optimization led to a smoother boundary at the re-entrant corner, and as a result, achieved lower maximum Hill's stress. It was also demonstrated that in contrast to solely considering characteristic parameters to design lattice structures, considering additional material and coating indicators during optimization resulted in optimized shape as well as the infill microstructures material distribution. This resulted in additional improvement for the strength-based optimized designs.

An issue that could be challenging for L-PBF-AM is the powder trapping for the 3D coated structures. While this issue was addressed for thin structures under 2D loading by removing the side coating, this solution is not suitable for thick part with 3D loading conditions. A potential solution could be considering the location and shape of the holes to remove the powder as design variables in the optimization process. As for performance requirements, only stiffness and strength were studied in this article. Buckling and fracture are important considerations, especially for lattice infill, that are subjects for future studies.

CRediT authorship contribution statement

Zhichao Wang: Visualization, Methodology, Validation, Writing - original draft. **Ali Y. Tamijan:** Conceptualization, Methodology, Supervision, Funding acquisition, Writing - review & editing.

Declaration of Competing Interest

The authors declare that they have no known competing financial interests or personal relationships that could have appeared to influence the work reported in this paper.

Data availability

Data will be made available on request.

Acknowledgments

The authors gratefully acknowledge the support of the National Science Foundation (NSF) under award number 1847133 with program

manager, Dr. Kathryn Jablokow.

References

- A. Clausen, N. Aage, O. Sigmund, Topology optimization of coated structures and material interface problems, Comput. Methods Appl. Mech. Eng. 290 (2015) 524–541, https://doi.org/10.1016/j.cma.2015.02.011.
- [2] B.S. Lazarov, O. Sigmund, Filters in topology optimization based on Helmholtztype differential equations, Int. J. Numer. Methods Eng. 86 (6) (2011) 765–781.
- [3] F. Wang, B.S. Lazarov, O. Sigmund, On projection methods, convergence and robust formulations in topology optimization, Struct. Multidiscip. Optim. 43 (6) (2011) 767–784.
- [4] A. Clausen, N. Aage, O. Sigmund, Exploiting additive manufacturing infill in topology optimization for improved buckling load, Engineering 2 (2) (2016) 250–257
- [5] A. Clausen, E. Andreassen, O. Sigmund, Topology optimization of 3D shell structures with porous infill, Acta Mech. Sin. 33 (4) (2017) 778–791, https://doi. org/10.1007/s10409-017-0679-2.
- [6] L. Lu, A. Sharf, H. Zhao, Y. Wei, Q. Fan, X. Chen, Y. Savoye, C. Tu, D. Cohen-Or, B. Chen, Build-to-last: strength to weight 3D printed objects, ACM Trans. Graph. 33 (4) (2014) 1–10.
- [7] V.-N. Hoang, P. Tran, N.-L. Nguyen, K. Hackl, H. Nguyen-Xuan, Adaptive concurrent topology optimization of coated structures with nonperiodic infill for additive manufacturing, Comput. -Aided Des. 129 (2020), 102918.
- [8] J. Wu, N. Aage, R. Westermann, O. Sigmund, Infill optimization for additive manufacturing – approaching bone-like porous structures, IEEE Trans. Vis. Comput. Graph. 24 (2) (2017) 1127–1140.
- [9] C. Dapogny, R. Estevez, A. Faure, G. Michailidis, Shape and topology optimization considering anisotropic features induced by additive manufacturing processes, Comput. Methods Appl. Mech. Eng. 344 (2019) 626–665, https://doi.org/ 10.1016/j.cma.2018.09.036.
- [10] O. Pantz, K. Trabelsi, A post-treatment of the homogenization method for shape optimization, SIAM J. Control Optim. 47 (3) (2008) 1380–1398.
- [11] J.P. Groen, J. Wu, O. Sigmund, Homogenization-based stiffness optimization and projection of 2D coated structures with orthotropic infill, Comput. Methods Appl. Mech. Eng. 349 (2019) 722–742, https://doi.org/10.1016/j.cma.2019.02.031.
- [12] P. Geoffroy-Donders, G. Allaire, G. Michailidis, O. Pantz, Coupled optimization of macroscopic structures and lattice infill, Int. J. Numer. Methods Eng. (2020).
- [13] Donders, P.G.Homogenization method for topology optmization of structures built with lattice materials. 2018.
- [14] L. Cheng, J. Bai, A.C. To, Functionally graded lattice structure topology optimization for the design of additive manufactured components with stress constraints, Comput. Methods Appl. Mech. Eng. 344 (2019) 334–359, https://doi. org/10.1016/j.cma.2018.10.010.
- [15] H. Yu, J. Huang, B. Zou, W. Shao, J. Liu, Stress-constrained shell-lattice infill structural optimisation for additive manufacturing, Virtual Phys. Prototyp. 15 (1) (2020) 35–48.
- [16] K. Gharibi, A.Y. Tamijani, Load-path-based topology optimization of twodimensional continuum structures, AIAA J. (2021) 1–10.
- [17] A.Y. Tamijani, S.P. Velasco, L. Alacoque, Topological and morphological design of additively-manufacturable spatially-varying periodic cellular solids, Mater. Des. (2020), 109155.
- [18] Z. Wang, A.Y. Tamijani, Computational synthesis of large-scale three-dimensional heterogeneous lattice structures, Aerosp. Sci. Technol. 120 (2022), 107258.
- [19] R.R. Fernandes, A.Y. Tamijani, Design optimization of lattice structures with stress constraints, Mater. Des. 210 (2021), 110026.
- [20] A. Clausen, E. Andreassen, On filter boundary conditions in topology optimization, Struct. Multidiscip. Optim. 56 (5) (2017) 1147–1155, https://doi.org/10.1007/ s00158-017-1709-1.
- [21] B.S. Lazarov, F. Wang, O. Sigmund, Length scale and manufacturability in density-based topology optimization, Arch. Appl. Mech. 86 (No. 1–2) (2016) 189–218, https://doi.org/10.1007/s00419-015-1106-4.
- [22] G.D. Cheng, X. Guo, ε-relaxed approach in structural topology optimization, Struct. Optim. 13 (4) (1997) 258–266, https://doi.org/10.1007/BF01197454.
- [23] P. Duysinx, and O. Sigmund, New developments in handling stress constraints in optimal material distribution. In: Proceedings of the 7th AIAA/USAF/NASA/ ISSMO Symposium on Multidisciplinary Analysis and Optimization. 1998, p. 4906.
- [24] K. Svanberg, The method of moving asymptotes-a new method for structural optimization, Int. J. Numer. Methods Eng. 24 (2) (1987) 359–373.
- [25] F. Hecht, New development in FreeFem++, J. Numer. Math. 20 (3–4) (2012) 251–266.